



# Visualization of surgical maneuvers using intraoperative real-time volumetric optical coherence tomography

JIANWEI D. LI,<sup>1</sup> CHRISTIAN VIEHLAND,<sup>1</sup> AL-HAFEEZ DHALLA,<sup>1</sup>  
ROBERT TROUT,<sup>1</sup>  WILLIAM RAYNOR,<sup>2</sup> ANTHONY N. KUO,<sup>1,2</sup>  
CYNTHIA A. TOTH,<sup>1,2</sup> LEJLA M. VAJZOVIC,<sup>2</sup> AND JOSEPH A.  
IZATT<sup>1,2,\*</sup>

<sup>1</sup>Department of Biomedical Engineering, 101 Science Drive, Durham, NC 27708, USA

<sup>2</sup>Department of Ophthalmology, Duke University Medical Center, 2351 Erwin Road, Durham, NC 27710, USA

\*joseph.izatt@duke.edu

**Abstract:** Ophthalmic microsurgery is traditionally performed using stereomicroscopes and requires visualization and manipulation of sub-millimeter tissue structures with limited contrast. Optical coherence tomography (OCT) is a non-invasive imaging modality that can provide high-resolution, depth-resolved cross sections, and has become a valuable tool in clinical practice in ophthalmology. While there has been substantial progress in both research and commercialization efforts to bring OCT imaging into live surgery, its use is still somewhat limited due to factors such as low imaging speed, limited scan configurations, and suboptimal data visualization. In this paper we describe, to the best of our knowledge, the translation of the fastest swept-source intraoperative OCT system with real-time volumetric imaging with stereoscopic data visualization provided via a heads-up display into the operating room. Results from a sampling of human anterior segment and retinal surgeries chosen from 93 human surgeries using the system are shown and the benefits that this mode of intrasurgical OCT imaging provides are discussed.

© 2023 Optica Publishing Group under the terms of the [Optica Open Access Publishing Agreement](#)

## 1. Introduction

Ophthalmic microsurgery is a technically demanding surgical discipline, which requires visualization through a stereoscopic microscope to accurately identify sub-millimeter tissue structures with subtle contrast, precisely manipulate those structures, and judge micro-architectural alterations [1]. These requirements are crucial to minimize residual tissue damage and maximize efficiency [2]. Unfortunately, the basic principles of ophthalmic surgical microscopes have remained unchanged for decades, and their limited depth perception, even when digitally augmented, and fixed visual perspective limits surgeon feedback. New complementary imaging techniques which take advantage of more modern technologies have the potential to improve real-time feedback and dramatically expand surgical capabilities.

Optical coherence tomography (OCT) is a non-invasive imaging technology which has become the gold standard in ophthalmology for diagnosis and management of ocular pathologies, due to its ability to generate micrometer-scale resolution, depth-resolved images of the eye [3–5]. Intraoperative OCT enables high-resolution visualization of intraocular structures that cannot be visualized through the microscope alone, tracking of surgical maneuvers, and verification of surgical goals, which could potentially impact intrasurgical decision making [6]. Our collaboration was among the first to demonstrate microscope-integrated intraoperative OCT in human surgeries, using a spectral-domain OCT (SD-OCT) system [7]. At the Cleveland Clinic, improvements such as electrically tunable focus were made to the OCT system and a heads-up display for visualization was added [8,9]. Such intraoperative systems have since

been commercialized with products such as the Zeiss Rescan 700 and Leica Enfocus [10,11]. However, these systems all utilized SD-OCT which has limited imaging speed and depth. More recently, our group demonstrated swept-source OCT (SS-OCT) at 100 kHz [12] with real-time 3D OCT visualization in human surgeries. We also reported an 800 kHz SS-OCT system using optical buffering and temporal spectral splitting, although this was limited to a technical demonstration and not utilized in human surgeries [13]. Lu et. al. demonstrated a 400 kHz SS-OCT intraoperative system employing post-objective injection of the OCT light, however this system lacked real-time visualization [14]. Several other groups have demonstrated MHz rate intraoperative OCT systems intended for neurosurgery or ophthalmic surgery, but have yet to demonstrate their utility in human studies [15–19].

In this work, we report on the translation of an intraoperative OCT system at 400 kHz that achieves, to our knowledge, the fastest live 4D (volumetric imaging through time) visualization of human ophthalmic microsurgery. Our system injects the OCT light into the infinity space of the surgical microscope above the objective, and was able to image, record, and render live 3D OCT volumes up to 7 volumes per second.

## 2. Methods

Our swept-source OCT engine (Fig. 1(a)) is based on a 400 kHz ping-pong laser (Axsun Technologies Inc.) operated at 1050 nm with a 100 nm sweep. Light from the laser was split using a 99/1 fiber coupler. The 1% arm of the fiber coupler was sent to a fiber Bragg grating (FBG) (O/E Land Inc.) and its reflection was detected by a photoreceiver (New Focus 1811, New Focus Inc.). This signal was used to generate trigger signals at the beginning of every wavelength sweep. The laser had a built-in k-clock, which was connected directly to a high-speed digitizer (ATS9373, Alazar Technologies Inc.). Mixed light transmitted through the transmissive reference arm and reflected from the sample was detected using a balanced photodetector (PDB481C-AC, Thorlabs, Inc.) and digitized at 1.8 GS/s using the high-speed digitizer. Computer-generated galvanometer drive waveforms were generated by analog outputs on a data acquisition (DAQ) card (PCIe-6323, National Instruments) and then relayed to the Mach-DSP servo driver board (Pangonlin Laser Systems Inc.). A retroreflector mounted on a motorized mechanical stage (A-LSQ150D-E01, Zaber Technologies Inc.) provided reference arm length adjustment over a 150 mm travel range which allowed for both anterior segment and retinal imaging. All of these components were built into a movable cart along with the computer (Fig. 1(b)). The portable engine was sufficiently robust to be routinely transported between storage, a wet laboratory for training and testing, and the Duke Eye Center operating rooms.

Our OCT sample arm (Fig. 1(c)) was based on a Leica Enfocus OCT scanner (Leica Microsystems Inc.). Standard optics in the scanner were replaced with optics optimized for 1050 nm light. A dichroic mirror coupled the 1050 nm OCT beam into the infinity space of the surgical microscope (Proveo 8, Leica Microsystems Inc.) above the microscope objective. Mechanical modifications were made to the metal backbone to accommodate high-speed galvanometer scanners (ScannerMAX Saturn 5B, Pangonlin Laser Systems Inc.) with 6 mm mirrors to support real-time volumetric (4D) OCT imaging. The OCT scanner was mounted on the surgical microscope. Rather than using the standard oculars with the microscope, an Alcon NGENUITY (Alcon Laboratories Inc.) camera was used to digitally capture the surgical microscope view and to enable heads-up digitally augmented stereo 3D viewing. Thus the standard surgical microscope view was simultaneously displayed alongside the OCT data using the Alcon NGENUITY 3D visualization system with a 4 K 3D display (see Fig. 1(c)). The OCT data was shown in real time with three different views: 3D volume, *en face* maximum intensity projection (MIP), and a user selected cross-sectional B-scan (Fig. 1(d)).

The OCT scanner contained optomechanical components which allowed for dynamic adjustment of the OCT focus to maintain parfocality with the microscope, as well as a motorized polarization

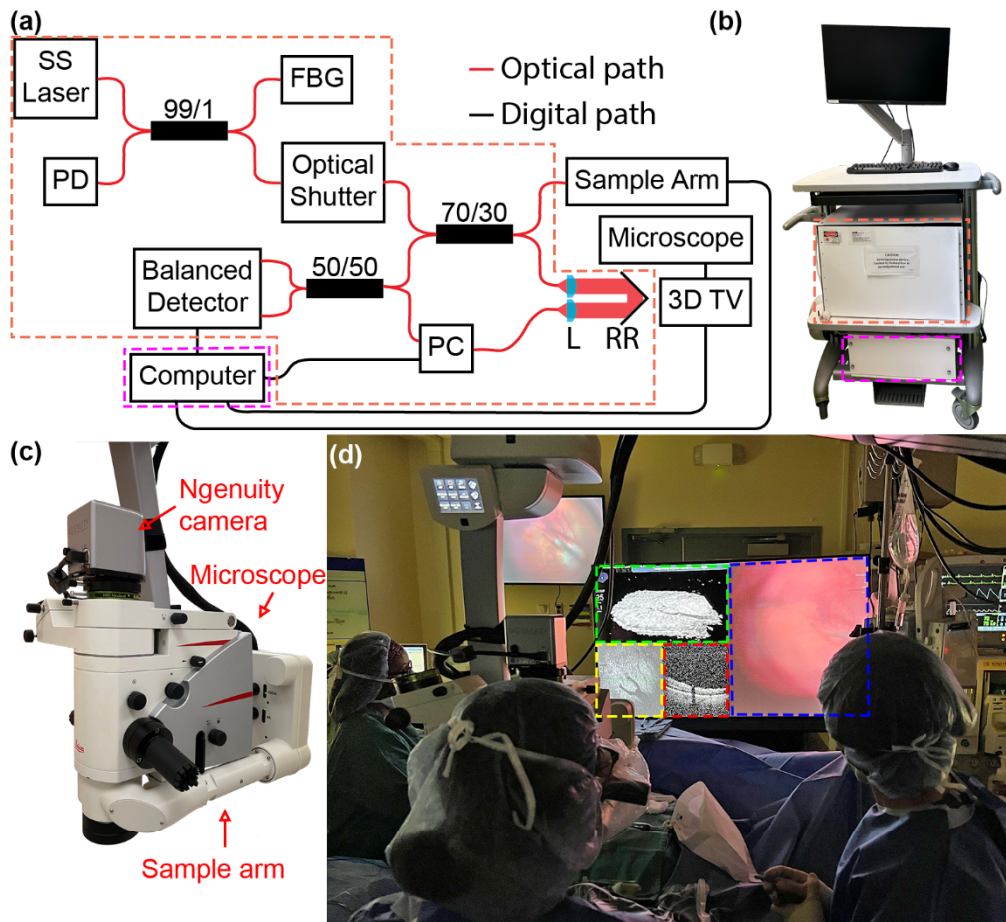


**Fig. 1.** (a) Duke intraoperative OCT system schematic with engine components indicated by dashed orange box and computer in dashed magenta box. FBG (fiber Bragg grating), PD (photodetector), PC (polarization controller), L (lens), RR (retroreflector). (b) OCT cart indicating location of the engine and computer with corresponding colored boxes. (c) OCT sample arm mounted on a Leica Proveo 8 surgical microscope with the NGENUITY 3D visualization system camera. (d) NGENUITY 3D visualization system display showing the OCT volume (dashed green box), MIP (dashed yellow box), and selected B-scan (dashed red box) and surgical microscope views (dashed blue box).

controller which allowed the operator to maximize the interference signal following system relocation. Anterior segment imaging was performed directly at the focal plane of the microscope. For retinal imaging, surgeons used indirect viewing systems such as the non-contact Oculus BIOM 5 (Oculus Surgical, Inc.) or a flat disposable contact lens (SKU: 55110, Oculus Surgical, Inc.). For both anterior segment and retinal imaging, the SS-OCT power measured at the cornea was maintained at less than 4.7 mW, which was within the allowable exposure limits specified by ISO 15004-2:2007 and IEC 60825:2001. An optical shutter built into the SS-OCT engine blocked the light when the system was not actively scanning.

A custom C/C++ application using CUDA (BROCT, Duke University) was used to collect, process, and render the OCT data in real-time [20]. The software also provided live adjustment of display contrast and visualization of the OCT data, as well as control of scan density, location, and field-of-view (FOV). The OCT scan location was controlled with a virtual joystick on the

operator computer screen. The movement of the virtual joystick generated a voltage offset which was combined with the normal galvanometer drive waveform using a summing amplifier. The system was configured with a variety of preset scan protocols covering different scan densities and FOVs as detailed in Table 1. While these presets covered the majority of imaging needs, some surgical situations demanded denser sampling or larger FOV. These parameters could be easily modified with the software. We used anisotropic scan protocols where there were significantly more A-scans/B-scan than B-scans/volume to produce B-scans of usable image quality at reasonable framerates. Since the surgical instruments typically were more closely aligned with the slow axis, this provided the best possible cross-section visualizations. However, this tradeoff did limit visualization of small structures in the fast axis. The FOVs used in this paper were chosen for several different reasons. Our minimum FOV was limited due to the safety considerations for light exposure, while the maximum FOV was limited by the performance of our galvanometer scanners. We have found that this range adequately covered the majority of our visualization needs. For fine, small-scale movements we used a smaller FOV which allowed the surgeon to see small features such as membranes. We used larger a larger FOV to visualize large-scale structures or movements where not as much resolution was needed to fit within the FOV and minimize the amount of manual tracking needed to follow the instrument. Additional applications from the vendor were used to provide real-time control of the electronic OCT focus (Leica Microsystems Inc.) and motorized fiber polarization controllers (Kinesis, Thorlabs Inc.). The computer used for processing and display had an Intel i9-9900X, with 64 GB of RAM, and an Nvidia RTX 3080 Ti for real-time SS-OCT signal processing and stereo volumetric OCT image rendering. The OCT data was first processed and rendered on the OCT system control computer, then sent to the NGENUITY visualization system over an HDMI cable. The frame rate of the OCT volumetric data and microscope camera differed quite significantly ( $\sim 7$  frames/second vs 60 frames/second, respectively). Furthermore, because the NGENUITY is a commercially available medical product and a relatively closed system, we were unable to directly synchronize the acquisition of the OCT and the microscope camera. We first characterized the performance of our OCT acquisition and processing by using Nsight Compute software (Nvidia Corporation) to determine the time between the start of each volume render. This was evaluated by performing 5 volume scans for each scan protocol, and these results are summarized in Table 1 as the mean volume rate (column 3). We also characterized the latency of both the surgical video stream as well as the OCT volume rendering by recording slow motion video at 240 fps of the entire setup while using it to image an infrared (IR) detector card (VRC5, Thorlabs, Inc.) and measuring the elapsed time between when a volume scan started as observed on the video recording of the IR card directly, and when the resulting data first appeared on the NGENUITY itself.

We first measured the latency of the surgical video stream by measuring the elapsed time between when the OCT light first appeared on the physical IR card to when it appeared in the

**Table 1. Preset scan protocols used in intraoperative OCT**

Scan density (A-scans/B-scan x B-scans/volume)	Nominal FOV (mm, in air)	Mean volume rate (Hz) and time/volume (ms) (n = 5)	Mean volumetric OCT display latency (ms) (n = 5)
340 × 80	3 × 3 anterior, 4 × 4 posterior	6.9 Hz and 144.9 ms, 6.8 Hz and 146.9 ms	120.8 ms, 125.8 ms
340 × 80	5 × 5 anterior, 7 × 7 posterior	7.5 Hz and 132.0 ms, 7.7 Hz and 129.6 ms	124.1 ms, 123.3 ms
340 × 80	8 × 8 anterior, 10 × 10 posterior	7.8 Hz and 128.0 ms, 7.2 Hz and 137.7 ms	133.3 ms, 110.0 ms
840 × 256	5 × 5 anterior, 7 × 7 posterior	1.63 Hz and 610.1 ms, 1.59 Hz and 625.6 ms	297.5 ms, 296.6 ms



surgical video window of the NGENUITY display. This was performed across all the listed scan protocols in Table 1, and we found the average to be  $91.1 \pm 5.1$  ms ( $n = 8$ ). We also characterized the mean latency of the entire OCT acquisition to display process. We used the same imaging setup and recorded the time between when the volume scan started on the physical IR card to when the corresponding section of the OCT volume appeared in the volumetric OCT display window on the NGENUITY display. We repeated this process 5 times for each scan protocol, and the results are summarized in the last column of Table 1. These reported latency times thus included the acquisition and processing time of the OCT data, as well as the data transmission and display on the NGENUITY itself.

All human research was performed under a study protocol (NCT03713268) approved by the Duke Medical Center Institutional Review Board and abided by the tenets of the Declaration of Helsinki. Patient consent to research participation was obtained prior to any research activities.

### 3. Results

We first characterized the performance of this new OCT system. To evaluate axial performance, we imaged a mirror through a neutral density filter. The results are shown in Fig. 2. Our system had an  $11.8 \mu\text{m}$  axial resolution (in air). The system sensitivity in anterior segment imaging mode was 94 dB with a maximum imaging depth of 7 mm (in air), and 6 dB falloff at 4.15 mm. The lateral resolution was measured as  $23 \mu\text{m}$  in the vertical axis and  $12 \mu\text{m}$  in the horizontal axis by imaging an USAF resolution target (R1DS1P, Thorlabs, Inc.) at the focal plane of the surgical microscope using  $840 \times 256$  A-scans/B-scans  $\times$  B-scans/volume over a  $5 \times 5$  mm FOV.

We chose to measure the lateral resolution using this scan protocol because this was our highest density scan. To characterize the resolution, we took an intensity profile across a square element on the test chart, and numerically calculated its derivative to derive the point spread function. A Gaussian was fitted to the point spread function and we calculated the FWHM of the Gaussian to derive the lateral resolution. The lateral resolution differs in the two different axes due to the anisotropic sampling, where we were limited by sampling density in the vertical axis rather than the actual optical resolution of the system. The measurements taken at the focal plane of the microscope are a direct measure of system resolution for anterior segment cases, but may not

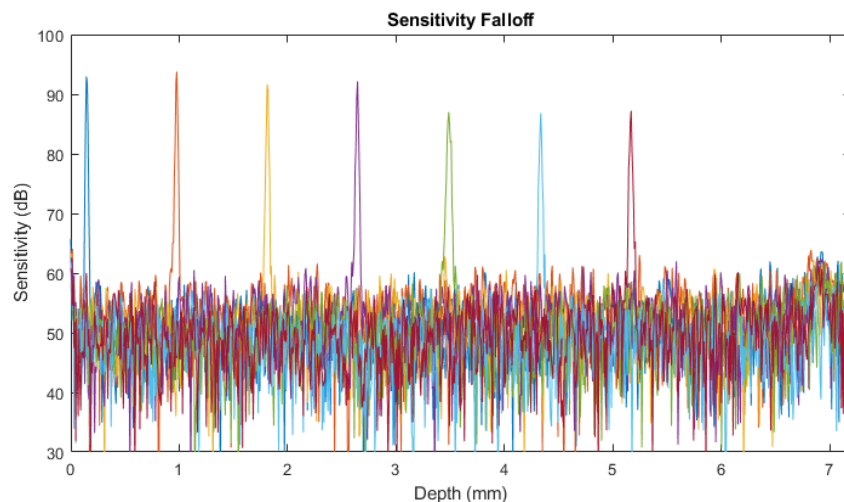


**Fig. 2.** System sensitivity falloff plot of our OCT system.  $11.8 \mu\text{m}$  axial resolution (in air), 94 dB peak sensitivity with 6 dB falloff at 4.15 mm.

accurately characterize the resolution at the retina which depends on the particular optics and aberrations of each patient's eye.

Ninety-three patients (mean  $\pm$  standard deviation of patient age:  $60 \pm 20$  years, 52 males, 41 females, 1 Asian, 19 Black or African American, 70 White, and 3 unknown) undergoing ophthalmic surgery at Duke University Medical Center were imaged with the investigational intraoperative OCT system. There were 86 retinal cases and 7 corneal cases. Out of the retinal cases, there were 31 epiretinal membrane surgeries, repair of 7 retinal detachments, closure of 19 macular holes, as well as a variety of other retinal pathologies. Out of the corneal cases, there were 3 cataract surgeries and 2 surgeries for corneal opacities. Multiple pathologies could be present in one case.

To start the imaging session, the surgeon adjusted the microscope until they had good visualization of the structures and were in focus at highest magnification. The OCT operator then adjusted the reference arm position and lateral scan location to visualize the region of interest. Once the region of interest was located, the OCT focus and polarization could be adjusted using software to optimize OCT imaging. These parameters required continual adjustment by a technician throughout the duration of the imaging session.

### 3.1. Intraoperative OCT imaging of human retinal surgery

Retinal microsurgery is used to treat a variety of pathologic conditions where the retina is damaged. One of the most common conditions is an epiretinal membrane, which is a semi-transparent tissue-like scar found on the inner surface of the retina and may lead to distortion or loss of vision. Surgical treatment involves a pars plana vitrectomy (PPV) where the vitreous is removed, and a variety of instruments such as forceps, diamond dusted membrane scrapers, and flexible loops can be used to remove epiretinal membranes. Another common pathology is retinal detachment where the retina lifts away from the underlying tissue of the eye and could lead to permanent vision loss if left untreated. Surgical treatment for retinal detachment also involves PPV followed by an injection of air, gas, or oil to tamponade a hole and allow the retina to reattach. Lastly, macular holes are a small break in the macula, which can affect vision. These are also treated by

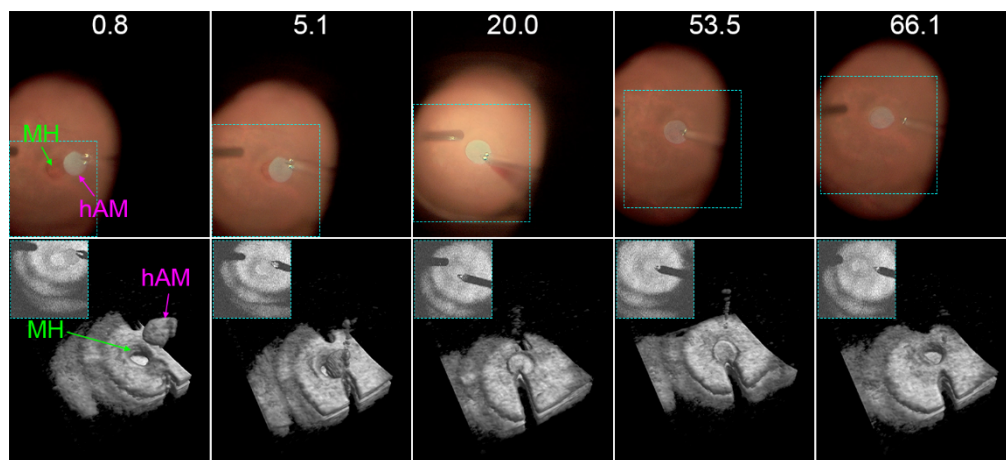


**Fig. 3.** Time sequence showing placement of human amniotic membrane (hAM) patch inside a macular hole (MH). Top row: surgical microscope view with time in seconds in white text. The dashed cyan box indicated FOV of the OCT scan. Bottom row: 3D OCT volumes with the maximum intensity projection (MIP) shown as insets in dashed cyan box. OCT scan parameters: 340 A-scans  $\times$  80 B-scans,  $5 \times 5$  mm. A video of this sequence can be found in [Visualization 1](#) and [Visualization 2](#).

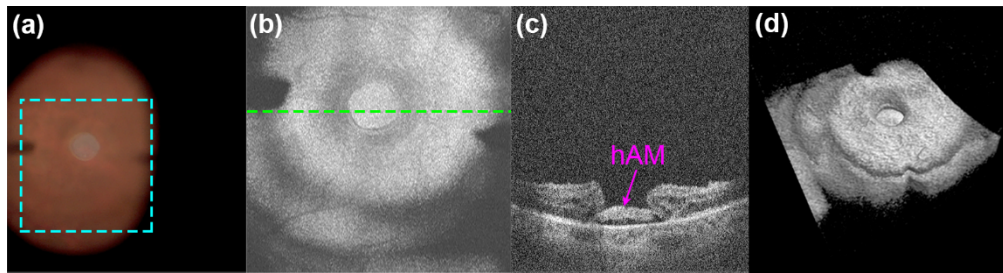


**Fig. 4.** Macular hole (MH) with human amniotic membrane patch (hAM) placed at the bottom of the hole. (a) Surgical microscope view with FOV of OCT indicated with the dashed cyan box. (b) OCT MIP with the (c) B-scan location indicated by the dashed green line. (d) 3D OCT volume. OCT scan parameters: 840 A-scans x 256 B-scans, 5 × 5 mm

performing a PPV, removing any membranes near the macular hole to release traction which may prevent the hole from closing, and exchanging the fluid in the eye with a gas to occlude the hole until it closes. Intraoperative OCT was used to provide additional visualization of such structures of interest.

In one case, a patient with a macular hole underwent a PPV and the internal limiting membrane (ILM) around the hole was removed. Next the surgeon attempted to place a human amniotic membrane (hAM) patch inside the macular hole. This technique can be used to promote closure of the macular hole and improve visual acuity [21]. With just a traditional surgical microscope view, it was difficult for the surgeon to assess the placement of the patch. However, with intraoperative OCT imaging the patch was clearly distinguishable from the surrounding tissue (Fig. 3).

With our custom software, we could easily change our scan configuration. In this case, the surgeon wanted to visualize the region of interest using a more densely sampled scan. We switched to a more densely sampled scan pattern and the surgeon quickly paused while OCT

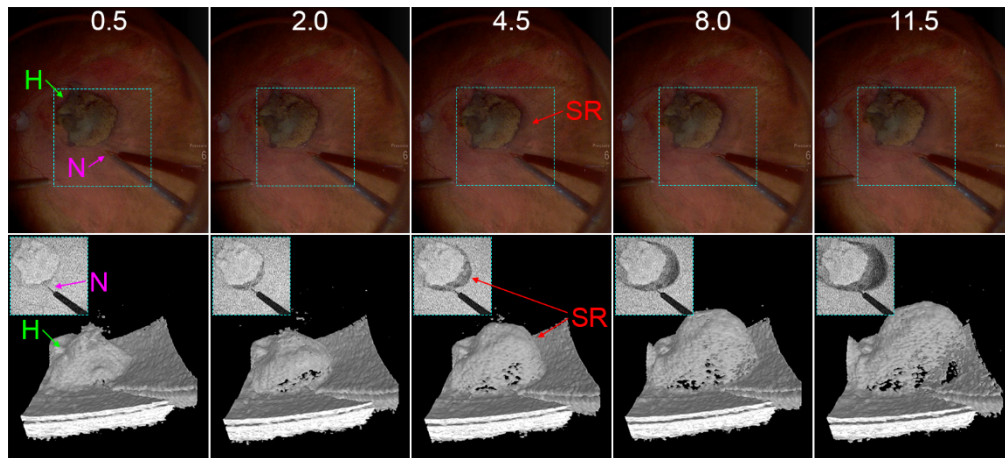


**Fig. 5.** Time sequence showing a subretinal injection (SR). The hemorrhage (H) is clearly visible in both the microscope view and surgical view as the needle (N) injects tPA. Top row: surgical microscope view with time in seconds in white text. The dashed cyan box indicated FOV of the OCT scan. Bottom row: 3D OCT volumes with the maximum intensity projection (MIP) shown as insets in dashed cyan box. OCT scan parameters: 340 A-scans x 80 B-scans, 7 × 7 mm. A video of this sequence can be found in [Visualization 3](#).

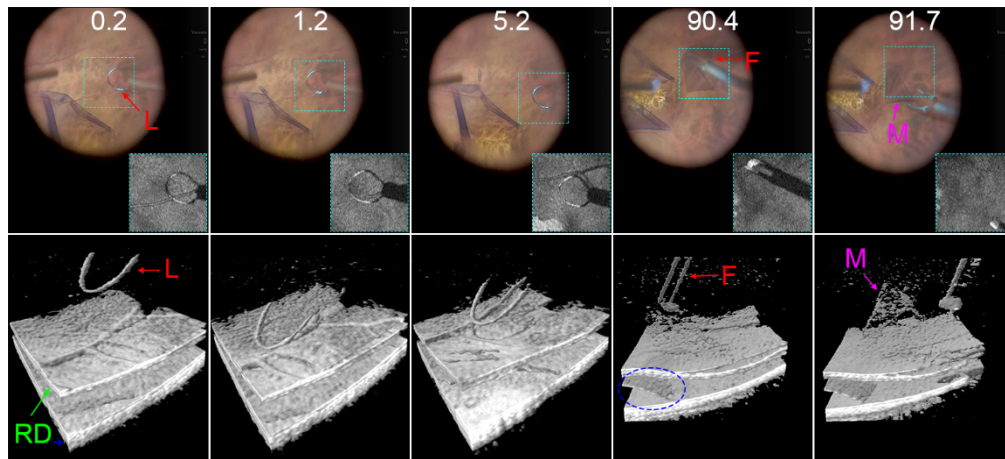


**Fig. 6.** Time sequence showing membrane peeling over a retinal detachment (RD). In the first 3 frames, a flex loop (L) was used. In the last 2 frames, the surgeon switched to ILM forceps (F) and the membrane (M) is clearly visible in the OCT volume. In the last 2 frames a possible schisis is seen in the OCT (dashed blue oval). Top row: surgical microscope view with time in seconds in white text. The dashed cyan box indicated FOV of the OCT scan. Bottom row: 3D OCT volumes with the maximum intensity projection (MIP) shown as insets in dashed cyan box. OCT scan parameters: 340 A-scans x 80 B-scans, 5 × 5 mm. A video of this sequence can be found in [Visualization 4](#) and [Visualization 5](#).

images were acquired. These scans (Fig. 4) provided valuable feedback to confirm completion of the surgical task that the patch was at the bottom of the hole.

In another case (Fig. 5), a patient with a subretinal hemorrhage and macular hemorrhage underwent vitrectomy. Following vitrectomy, the surgeon performed a subretinal injection of tissue plasminogen activator (tPA). These tPA injections can be used to displace the hemorrhage from the fovea [22]. The OCT view can be used to confirm placement of the needle in subretinal space. Furthermore, while the extent of the injection was visible on the standard microscope view, it was greatly enhanced with the 3D OCT view, providing surgeons with visual feedback on the volume of the injection in real-time. In addition to providing visualizations of the injection, we also describe performing quantitative measurements of subretinal injection volume in section 3.2.

A final example of a retinal case was a patient presenting with macula-off retinal detachment (Fig. 6). The surgeon performed a vitrectomy and stained the ILM using Trypan Blue. The contrast was necessary for the surgeons to distinguish the membranes from the surrounding tissue. However, OCT was also able to image these membranes. A flex loop and ILM forceps were both used in this case to peel membrane in order to relieve tension and allow the retina to return to its proper position. The OCT was also able to identify a possible schisis that was not apparent on the standard microscope view.

### 3.2. Quantitative analyses using intraoperative OCT

While we have shown visualizations of a wide range of cases, we can also use the data from intraoperative OCT to perform quantitative analyses. Two such applications are demonstrated in this paper. First, we performed quantitative measurements of a subretinal tPA injection (Fig. 7). The surgeon performed the procedure as described in the previous section. Using special measurement techniques that our group has previously developed, we were able to optically model our OCT system and the patient's eye to determine the voxel dimensions in the OCT volume [23].



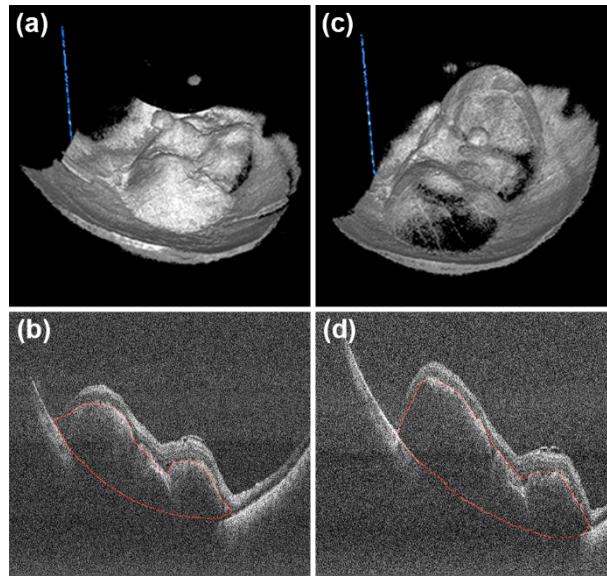


**Fig. 7.** (a) Volumetric and (b) B-scan view of the submacular hemorrhage. (c) Volumetric and (d) B-scan view of the subretinal injection over the submacular hemorrhage. The blue line in the volumetric views indicated the location of the corresponding B-scan. The segmented region of interest in the B-scan is outlined in red. OCT scan parameters: 750 A-scans x 750 B-scans, 15 × 15 mm.

A region of interest was segmented and the volume of the voxels within the region was determined. In this case, we measured the volume of the existing submacular hemorrhage (Fig. 7(a)-(b)) to be 100  $\mu\text{L}$  and after the subretinal injection (Fig. 7(c)-(d)) to be 218  $\mu\text{L}$ . Therefore, the subretinal injection volume measured using OCT was the difference between the two volumes, or 118  $\mu\text{L}$ . The amount as measured by the surgeons using the markings on the injection syringe was 130  $\mu\text{L}$ . The 9% difference in volume could be due to delivery into the vitreous, efflux, or other human

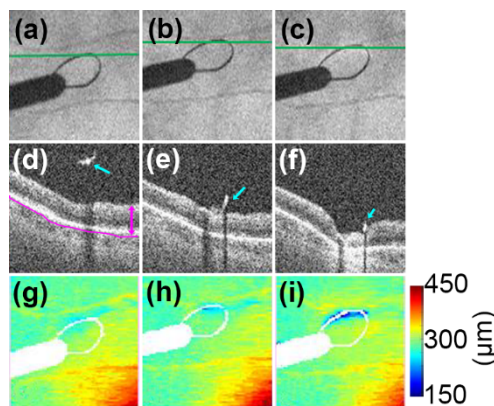


**Fig. 8.** (a-c) MIP view including the surgical tool and retina with the corresponding (d-f) B-scans indicated by the green line. The cyan arrow indicates the position of the surgical tool. The magenta line indicates the segmented retina and the arrow indicates the retinal thickness. (g-i) Retinal thickness map over the entire volume, where thinning is indicated in blue and thickening in red. OCT scan parameters: 340 A-scans x 80 B-scans, 3 × 3 mm.

error. This highlights the value that intraoperative OCT can bring, since accurate measurement of subretinal injection volume is critical to ensure proper delivery of therapeutics as well as evaluating safety and efficacy.

Secondly, we demonstrated extraction of quantitative measurements of tool-tissue interactions in surgery (Fig. 8). The volumes were segmented using custom software developed at Duke (DOCTRAP) into surgical tools and retina [24]. With the retina segmented, we produced a retinal thickness map that shows deformation events as the tool presses down during a surgical maneuver. Such information could produce useful insight into techniques for retinal surgery.

While these examples are currently performed in post-processing, we believe they demonstrate the feasibility of such analyses using data acquired from an intraoperative OCT system. With additional improvements in real-time automated segmentation and registration, this work could potentially be extended to use during live surgery.

### 3.3. Intraoperative OCT imaging of human anterior segment surgery

Anterior segment surgeries, which include cataract surgery and corneal transplants, are among the most commonly performed surgeries in the US. Cataracts are a clouding of the lens resulting in blurriness and decreased contrast and color vision. Cataracts can be treated surgically by replacing the clouded natural lens with an artificial intraocular lens (IOL). Corneal transplants are used to treat a variety of problems with the cornea, including disease, injury, and scarring which compromise the cornea's role in vision. These procedures are incredibly common, and there is potential for OCT visualizations to be used to guide decision making. Some examples of this are explored in this section.

In one case (Fig. 9), a patient with a central corneal opacity underwent a full thickness corneal transplant (penetrating keratoplasty, PK). A trephine was used to create a circular cut around the center of the damaged cornea so it could be removed. The donor cornea was then positioned in place and a series of sutures were placed around the entire circumference to secure the donor graft to the host cornea. However, there is evidence that suture placement and variable tension may impact post-operative visual acuity and astigmatism. Currently corneal topography scans are one method of managing astigmatism by visualizing the way the sutures deform the cornea [25–27]. Real-time volumetric OCT could potentially allow such corrections to happen during surgery.

Another common pathology is a nuclear sclerotic cataract. The natural lens becomes cloudy causing deteriorating vision, and thus must be removed. A common technique to accomplish this is to use an ultrasonic phacoemulsification probe to break up the lens within the capsular bag. The smaller pieces can then be extracted. However, one of the challenges with this technique is assessing if the phaco groove depth is adequate. If the groove is not deep enough, the nucleus does not split which complicates additional attempts. On the other hand, if the groove is too deep, there is potential for a posterior capsule rupture. Traditionally, the groove depth is determined using visual cues such as changes in the red-light reflex or the appearance of striations in the groove [28]. These cues are not precise, but the ability of OCT imaging to provide cross-sectional views is valuable for showing the actual depth (Fig. 10). While these cross-sectional views currently only provide qualitative information, the current standard is also a qualitative assessment. Furthermore, it is feasible that real-time automated segmentation could be developed to enable this measurement during surgery. Before the case begins, for example, the lens thickness could be measured using OCT to serve as a reference depth for how deep the surgeon could safely make the phaco groove. While these images of the phaco groove may not necessarily be needed by an experienced surgeon performing an average cataract case, it could be valuable for training new surgeons or when performing atypical cases.

For the final case, we had a patient with intermediate uveitis and secondary aphakia due to a compromised posterior capsule during primary cataract surgery. To treat the aphakia, a 3-piece

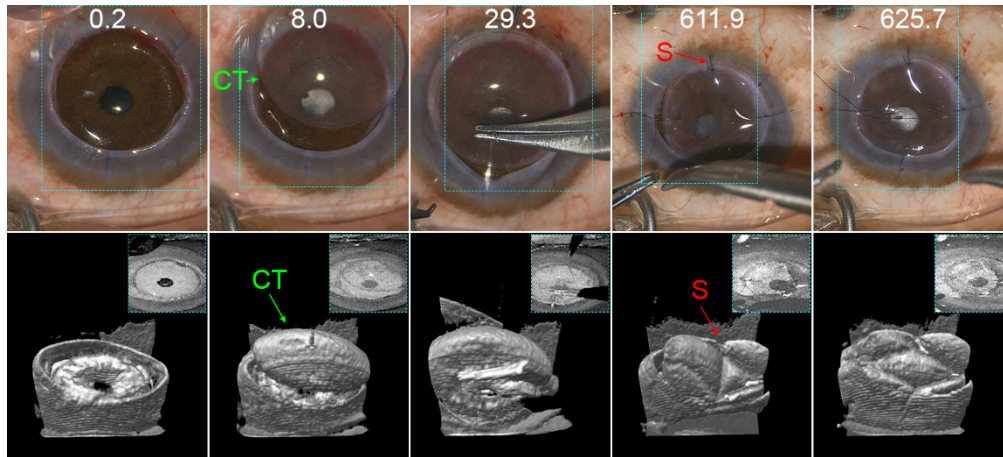


**Fig. 9.** Time sequence showing a corneal transplant (CT) being sutured (S) into place. Top row: surgical microscope view with time in seconds in white text. The dashed cyan box indicated FOV of the OCT scan. Bottom row: 3D OCT volumes with the maximum intensity projection (MIP) shown as insets in dashed cyan box. OCT scan parameters: 340 A-scans x 80 B-scans,  $15 \times 15$  mm. A video of this sequence can be found in [Visualization 6](#) and [Visualization 7](#).

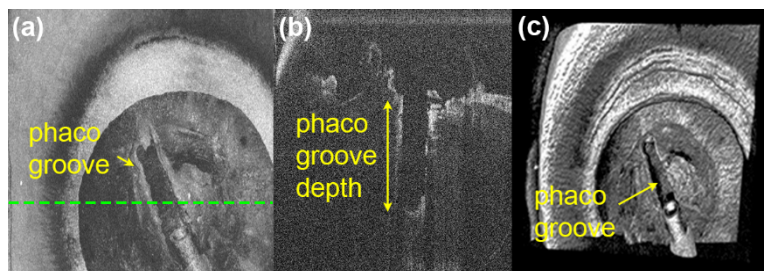


**Fig. 10.** (a) OCT MIP with the (b) B-scan location indicated by the dashed green line. (c) 3D OCT volume. OCT scan parameters: 840 A-scans x 256 B-scans,  $8 \times 8$  mm

IOL (CT Lucia 602, Zeiss Group) was inserted with the intent to optic capture the lens, meaning have the central optic (acrylic) of the IOL behind the lens capsule for anatomic positioning while having the haptics (polyvinylidene fluoride) anterior and in the sulcus for support in the absence of an intact posterior capsule. We can quickly pause and acquire a high-resolution OCT scan over a large FOV, and with these images (Fig. 11), the surgeon can confirm the position of the optic and haptics relative to the anterior capsule and also to evaluate the tilt of the IOL relative to the rest of the eye. Such an assessment would be difficult to make with just the surgical microscope view.

While the data shown in the last two cases are higher density scans, they can still be processed and rendered fast enough to be of clinical value. The features of interest being imaged here are also large enough where a fast scan would feasibly still provide enough quality to be useful. Furthermore, depending on the situation, surgeons may want to pause, take a single high-density scan, and evaluate multiple B-scans throughout the volume.

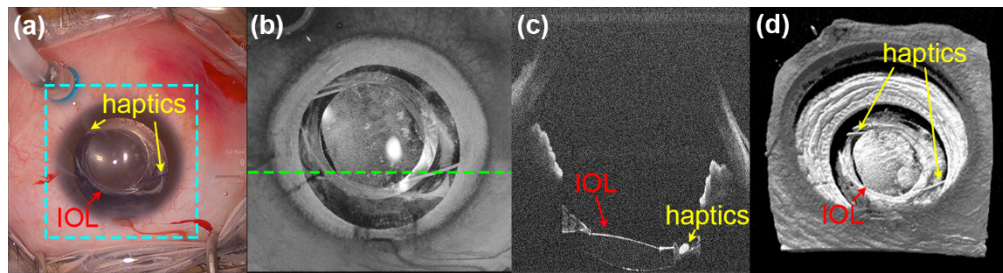


**Fig. 11.** Placement of 3-piece intraocular lens (IOL) with optic capture (optic of IOL behind anterior capsule with haptics anterior and in the sulcus) due to a compromised posterior capsule. (a) Surgical microscope view with FOV of OCT indicated with the dashed cyan box. (b) OCT MIP with the (c) B-scan location indicated by the dashed green line. (d) 3D OCT volume. OCT scan parameters: 750 A-scans x 750 B-scans,  $15 \times 15$  mm

#### 4. Discussion and conclusion

In this paper, we have presented an intraoperative OCT system capable of versatile 4D imaging. This system can be configured to perform imaging in the anterior segment or retina with a variety of different scan densities and speeds. We captured OCT data from a diverse range of human ophthalmic surgical cases. This OCT data was displayed as 3D volumes, *en face* MIPs, and cross-sectional B-scans alongside the traditional surgical microscope view.

We aimed to highlight the utility and benefits that real-time volumetric OCT imaging can provide compared to the traditional microscope view alone. We believe that 4D is particularly useful in visualizing dynamic surgical movements and assessing the position structures and features of interest in cases such as patching macular holes, performing subretinal injections, membrane peels, or corneal transplants. On the other hand, cross-sectional B-scans were valuable in determining precise location of surgical instruments or other structures of interest as shown in the macular hole patch, cataract surgery, and placing IOLs. The *en face* MIP served as a good reference to the normal surgical microscope view to help the surgeon orient themselves with where the OCT data is being captured. Furthermore, while OCT imaging appears to provide valuable visualizations that otherwise would not be seen with the standard microscope view, the introduction of this additional modality opens the possibility of making quantitative analyses such as subretinal injection volume, retinal thickness maps, or phaco groove depths. Such visualizations and quantitative analyses could be particularly beneficial for training new surgeons and in atypical cases.

While this current system appears to provide benefits over the state of the art, there are several major improvements which could be made. The material and finish of each individual surgical instrument, as well as its position and orientation had a significant impact on its visibility in OCT. Currently, many surgical instruments are not well suited for OCT imaging, as they were not designed with OCT compatibility as a priority. In some imaging situations, the tool itself may be outside the imaging depth or oriented at a steep angle, so the tool itself was not imaged and the underlying tissue is shadowed. We suggest that there are interesting avenues for future work in developing more OCT compatible instruments to enable better visualization of tool-tissue interactions. For example, a more reflective tool surface would allow the tool itself to show up on OCT but would shadow the underlying tissue. Alternatively, a more transmissive material would allow for better visualization of the tissue underneath at the expense of visualization the tool itself. However, even with the existing commercially available tools, in some cases such as the macular hole repair, visualization of the tool is not strictly needed as the primary feature of interest is the amniotic membrane which is visible on OCT. Another such improvement would



be increased imaging depth. We noted that for cataract cases, we were not able to consistently visualize the cornea all the way down to the posterior capsule. Increased imaging depth would further improve the utility of our system in such cases since the surgeon is looking to go as deep as possible without rupturing the posterior capsule. Additionally, while our current volume rate is fast enough to be usable, going to a faster line rate would improve ease of use for the surgeon. Currently, we must make some tradeoff between sampling density and volume rate. Faster line rates would allow us to increase the sampling density potentially leading to improved visualization of smaller structures such as epiretinal membranes without comprising volume rate. Alternatively, we could maintain the same sampling density and increase the volume rate allowing the surgeon to operate more fluidly since the OCT rate will be closer to that of the surgical microscope. Additionally, an experienced operator is needed to fully leverage the benefits of the intraoperative OCT system, since they must manually perform axial and lateral tracking, adjust the volume orientation, as well as constantly optimize polarization and electronic focus. Currently, the operator must constantly adjust the reference arm length to keep the image within the imaging range. Typically, they also laterally track the tip of the surgical instrument such that it is the displayed B-scan, unless requested otherwise by the surgeon. For example, in some cases the surgeon may ask to go through all the B-scans in a volume when looking for features such as residual membranes. The volume renderings have a default orientation which the surgeons can ask to change as needed to visualize a feature. Automating these adjustments could significantly reduce the amount of work needed by the operator, increasing ease of use. Additionally, this would also provide better visualizations throughout the case since these tasks could happen in parallel reducing the amount of time the surgeon spends looking at an image that has not been fully optimized or tracked to the right location. With these improvements, it is feasible that the system could be run entirely by the surgeon, further increasing clinical utility.

**Funding.** National Institutes of Health (U01EY028079).

**Acknowledgments.** We would like to thank the staff at the Duke Eye Center for their support of this project.

**Disclosures.** AD: Duke University (P), CZ: Duke University (P), CAT: Duke University Medical Center (P), Alcon Laboratories (R), Theia Imaging (I,C), Emmes (C), LMV: Duke University Medical Center (P), Alcon Inc. (F,C), JAI: Duke University (P)

**Data availability.** Data underlying the results presented in this paper are not publicly available at this time due to privacy reasons.

## References

1. M. Singh and A. Saxena, "Microsurgery: A Useful and Versatile Tool in Surgical Field," *Surgery: Curr. Res.* **04**(04), 4 (2014).
2. S. Ramachandran, A. M. Ghanem, and S. R. Myers, "Assessment of microsurgery competency-where are we now?" *Microsurgery* **33**(5), 406–415 (2013).
3. D. Huang, E. A. Swanson, C. P. Lin, J. S. Schuman, W. G. Stinson, W. Chang, M. R. Hee, T. Flotte, K. Gregory, C. A. Puliafito, and J. G. Fujimoto, "Optical Coherence Tomography," *Science* **254**(5035), 1178–1181 (1991).
4. J. A. Izatt, M. R. Hee, E. A. Swanson, C. P. Lin, D. Huang, J. S. Schuman, C. A. Puliafito, and J. G. Fujimoto, "Micrometer-Scale Resolution Imaging of the Anterior Eye In Vivo With Optical Coherence Tomography," *Arch. Ophthalmol.* **112**(12), 1584–1589 (1994).
5. C. A. Puliafito, M. R. Hee, C. P. Lin, E. Reichel, J. S. Schuman, J. S. Duker, J. A. Izatt, E. A. Swanson, and J. G. Fujimoto, "Imaging of Macular Diseases with Optical Coherence Tomography," *Ophthalmology* **102**(2), 217–229 (1995).
6. O. M. Carrasco-Zevallos, B. Keller, C. Viehland, L. Shen, M. I. Seider, J. A. Izatt, and C. A. Toth, "Optical Coherence Tomography for Retinal Surgery: Perioperative Analysis to Real-Time Four-Dimensional Image-Guided Surgery," *Invest. Ophthalmol. Visual Sci.* **57**(9), OCT37–OCT50 (2016).
7. Y. K. Tao, J. P. Ehlers, C. A. Toth, and J. A. Izatt, "Intraoperative spectral domain optical coherence tomography for vitreoretinal surgery," *Opt. Lett.* **35**(20), 3315–3317 (2010).
8. Y. K. Tao, S. K. Srivastava, and J. P. Ehlers, "Microscope-integrated intraoperative OCT with electrically tunable focus and heads-up display for imaging of ophthalmic surgical maneuvers," *Biomed. Opt. Express* **5**(6), 1877–1885 (2014).

9. Y. Tao, M. El-Haddad, S. Srivastava, D. Feiler, A. Noonan, A. Rollins, and J. Ehlers, *Intraoperative optical coherence tomography using an optimized reflective optical relay, real-time heads-up display, and semitransparent surgical instrumentation*, SPIE BiOS (SPIE, 2015), Vol. 9312.
10. “OPMI LUMERA 700 - Surgical Microscopes - Retina - Zeiss,” retrieved <https://www.zeiss.com/meditec/us/products/ophthalmology-optometry/retina/therapy/surgical-microscopes/opmi-lumera-700.html>.
11. “Intraoperative OCT imaging system EnFocus - Leica,” retrieved <https://www.leica-microsystems.com/products/surgical-microscopes/p/enfocus/>.
12. O. M. Carrasco-Zevallos, B. Keller, C. Viehland, L. Shen, G. Waterman, B. Todorich, C. Shieh, P. Hahn, S. Farsiu, A. N. Kuo, C. A. Toth, and J. A. Izatt, “Live volumetric (4D) visualization and guidance of in vivo human ophthalmic surgery with intraoperative optical coherence tomography,” *Sci. Rep.* **6**(1), 31689 (2016).
13. O. Carrasco-Zevallos, C. Viehland, B. Keller, A. Kuo, C. Toth, and J. Izatt, *High-speed 4D intrasurgical OCT at 800 kHz line rate using temporal spectral splitting and spiral scanning (Conference Presentation)*, SPIE BiOS (SPIE, 2017), Vol. 10053.
14. C. D. Lu, N. K. Waheed, A. Witkin, C. R. Bauman, J. J. Liu, B. Potsaid, A. Joseph, V. Jayaraman, A. Cable, K. Chan, J. S. Duker, and J. G. Fujimoto, “Microscope-Integrated Intraoperative Ultrahigh-Speed Swept-Source Optical Coherence Tomography for Widefield Retinal and Anterior Segment Imaging,” *Ophthalmic Surgery Lasers and Imaging Retina* **49**(2), 94–102 (2018).
15. Y. Miura, W. Draxinger, C. Grill, T. Pfeiffer, S. Grisanti, and R. Huber, “MHz-OCT for low latency virtual reality guided surgery: First wet lab experiments on ex-vivo porcine eye,” in *Clinical and Preclinical Optical Diagnostics II*, SPIE Proceedings (Optica Publishing Group, 2019), 11078\_11013.
16. D. Theisen-Kunde, W. Draxinger, M. M. Bonsanto, P. Streng, N. Detrez, R. Huber, and R. Brinkmann, “1.6 MHz FDML OCT for Intraoperative Imaging in Neurosurgery,” in *European Conferences on Biomedical Optics 2021 (ECBO)*, OSA Technical Digest (Optica Publishing Group, 2021), ETu4A.2.
17. J. P. Kolb, W. Draxinger, J. Klee, T. Pfeiffer, M. Eibl, T. Klein, W. Wieser, and R. Huber, “Live video rate volumetric OCT imaging of the retina with multi-MHz A-scan rates,” *PLoS One* **14**(3), e0213144 (2019).
18. W. Draxinger, Y. Miura, C. Grill, T. Pfeiffer, and R. Huber, “A real-time video-rate 4D MHz-OCT microscope with high definition and low latency virtual reality display,” in *Clinical and Preclinical Optical Diagnostics II*, SPIE Proceedings (Optica Publishing Group, 2019), 11078\_11071.
19. A. Britten, P. Matten, J. Weiss, M. Niederleithner, H. Roodaki, B. Sorg, N. Hecker-Denschlag, W. Drexler, R. A. Leitgeb, and T. Schmolz, “Surgical microscope integrated MHz SS-OCT with live volumetric visualization,” *Biomed. Opt. Express* **14**(2), 846–865 (2023).
20. C. Viehland, B. Keller, O. M. Carrasco-Zevallos, D. Nankivil, L. Shen, S. Mangalesh, D. T. Viet, A. N. Kuo, C. A. Toth, and J. A. Izatt, “Enhanced volumetric visualization for real time 4D intraoperative ophthalmic swept-source OCT,” *Biomed. Opt. Express* **7**(5), 1815–1829 (2016).
21. T. Caporossi, B. Pacini, D. Bacherini, F. Barca, F. Faraldi, and S. Rizzo, “Human amniotic membrane plug to promote failed macular hole closure,” *Sci. Rep.* **10**(1), 18264 (2020).
22. C. L. Haupt, B. W. McCuen, G. J. Jaffe, E. R. Steuer, T. A. Cox, C. A. Toth, S. Fekrat, and E. A. Postel, “Pars plana vitrectomy, subretinal injection of tissue plasminogen activator, and fluid–gas exchange for displacement of thick submacular hemorrhage in age-related macular degeneration,” *Am. J. Ophthalmol.* **131**(2), 208–215 (2001).
23. J. D. Li, W. Raynor, A.-H. Dhalla, C. Viehland, R. Trout, C. A. Toth, L. M. Vajzovic, and J. A. Izatt, “Quantitative measurements of intraocular structures and microinjection bleb volumes using intraoperative optical coherence tomography,” *Biomed. Opt. Express* **14**(1), 352–366 (2023).
24. J. Y. Lee, S. J. Chiu, P. P. Srinivasan, J. A. Izatt, C. A. Toth, S. Farsiu, and G. J. Jaffe, “Fully automatic software for retinal thickness in eyes with diabetic macular edema from images acquired by cirrus and spectralis systems,” *Invest. Ophthalmol. Visual Sci.* **54**(12), 7595–7602 (2013).
25. G. Ho Wang Yin and L. Hoffart, “Post-keratoplasty astigmatism management by relaxing incisions: a systematic review,” *Eye and Vis* **4**(1), 29 (2017).
26. R. Subrahmanyam, A. Liu, W. Raynor, J. D. Li, R. P. McNabb, C. A. Toth, J. Izatt, and A. N. Kuo, “MIOCT-generated topography maps for astigmatism magnitude and axis calculation in corneal phantoms,” *Invest. Ophthalmol. Visual Sci.* **62**, 2017 (2021).
27. A. Hoang, J. D. Li, W. Raynor, J. A. Izatt, C. A. Toth, A. N. Kuo, and M. B. Daluvoy, “Real-Time 3D Microscope-Integrated OCT and Display during Keratoplasty,” in *ASCRS*, (Las Vegas, 2021).
28. K. Dunne and A. J. Buller, “Measuring phacoemulsification groove depth using probe tip dimensions and biometry lens thickness readings,” *Clin. Ophthalmol.* **10**, 1553–1556 (2016).